Electronic properties of the five principal stackings of boron nitride moiré bilayers

Sylvain Latil, Hakim Amara, Lorenzo Sponza

Electronic properties of the five principal stackings of boron nitride moiré bilayers

Sylvain Latil,[1] Hakim Amara,[2,3] and Lorenzo Sponza[2,4]

[1] *CEA, IRAMIS, SPEC, GMT, 91191 Gif-sur-Yvette, France*
[2] *Université Paris-Saclay, ONERA, CNRS, Laboratoire d'étude des microstructures (LEM), 92322, Châtillon, France*
[3] *Université de Paris, Laboratoire Matériaux et Phénomènes Quantiques (MPQ), CNRS-UMR7162, 75013 Paris, France*
[4] *European Theoretical Spectroscopy Facility (ETSF), B-4000 Sart Tilman, Liège, Belgium*

(Dated: June 14, 2022)

All theoretical calculations on boron nitride moiré bilayers report the properties of, at most, two possible stackings which preserve the monolayer hexagonal symmetry (i.e. the invariance upon rotations of 120°). In this work, we demonstrate that, for a given moiré periodicity, the same symmetry is respected by five different stackings and not only two as always discussed in literature. We introduce some definitions and an appropriate nomenclature to identify unambiguously the twist angle and the stacking sequence of any BN bilayer with order-3 rotation symmetry. The nomenclature we introduce here and the method to calssify stacking sequences and the angles is completely general and can be applied to homobilayers of any hexagonal 2D materials. Moreover, we produce density functional theory predictions of the electronic structure of each of the five stacking sequences at six different twist angles and discuss the evolution of the gapwidth and band structure and as a function of these parameters. We show that the gap is indirect at any angle and in any stacking and we identify features that are conserved at any angle within the same stacking sequence.

Initiated by twisted bilayer graphene, moiré systems formed by 2D atomic layers have recently been established as a unique playground for highlighting novel and fascinating properties [1]. A tiny twist between the two van der Waals atomic layers can modify deeply their electronic properties. In the case of graphene bilayers, a moiré mini-band with flat dispersion appears whenever the layers are stacked at specific twist angles, called magic angles [2, 3]. Such a feature enhances the effects of electron interaction, thus opening up new perspectives for the exploration of highly correlated systems [4–6].

In twisted bilayers formed of gapped materials (e.g. semiconducting transition metal dichalcogenides) the formation of moiré flat bands has an impact on the optical properties. For instance, recent experiments demonstrate that the twist angle can be used as a knob to modulate the exciton lifetime [7], or the energy and intensity of emitted light [8–11]. Moreover specific orientation conditions are not required to form flat bands [12–14]. This is still true for hexagonal boron nitride (hBN) which is a key compound in 2D materials research. In contrast to graphene, hBN is a wide band gap semiconductor (> 6 eV) [15, 16] and is therefore attracting interest for its strong photoluminescence properties [17, 18]. Strong excitonic effects have already been observed in the bulk and even more important effects are predicted in single layers where optical properties are expected to be driven by excitons [19]. Recently, experimental techniques inherited from graphene studies have been applied to the fabrication of bilayers of hBN with a controlled twist angle to achieve engineered ferroelectrics, thus expanding the capabilities of 2D materials for various applications [20, 21]. Regarding optical properties of hBN bilayers, Lee and coworkers [22] observed an increase of the luminescence intensity and a decrease of the moiré sub-band gapwidth for increasing twist angles. From the standpoint of atomistic simulations, geometries of stackings with a small angle of rotation require very large periodic cells (order of thousands of atoms), but numerical approaches based on self-consistent calculations are rather limited to some hundreds of atoms in the calculation cell [23]. As for graphene [2, 24], tight-binding (TB) or continuous models based on $k \cdot p$ approximations are more adapted to deal with very large systems and have therefore been developed [6, 14, 25, 26]. However, detailed results for the electronic structure as a function of the twist angle are still lacking. More precisely, the very nature of the band gap is still not elucidated/discussed while it obviously strongly drives the optical and excitonic properties of monolayer and bulk BN [15, 16, 27]. In the case of untwisted BN bilayers, it has been shown that the long range interplanar interaction, and hence the stacking sequence [28, 29], strongly influences the character of the gap [19, 28]. However, all stacking geometries existing in such heteregenous twisted BN structures, which are much more complex, were not addressed.

In this Letter, we want to investigate the electronic structure of twisted BN bilayers by taking into account fully and on the same footing its dependence on the twist angle and the stacking sequence. As a first step, we demonstrate the existence of five and only five different stacking possibilities to construct BN bilayers with order-3 symmetry and provide a non-ambiguous nomenclature that can be applied to untwisted configurations and to any other homo-bilayer formed of hexagonal 2D materials. From this symmetry analysis, we investigated the evolution of the band structure as a function of the twist angle for each of the five stackings with density functional theory (DFT) paying a special attention to the indirect nature of the band gap.

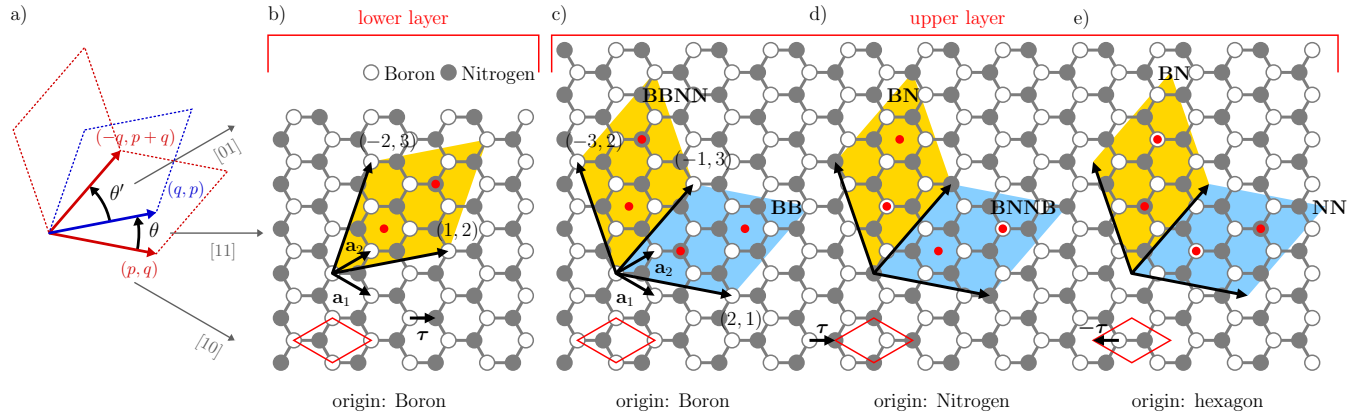

FIG. 1. a) Graphical representation of θ and θ' angles according to the (p, q) integers. b) The lower layer supercell is always the (q, p) with a boron atom at the origin. In our example $p = 2$ and $q = 1$. c) d) and e) the three (p, q) supercells of the upper layer in yellow with respectively B, N or hexagon at the origin, and in blue the correspnding $(-q, p + q)$ supercells.

The usual way to construct a tiling of rotated bilayers that preserves long range translational symmetries, is to place the two layers into coincident supercells. Let us take a honeycomb lattice with primitive vectors $\mathbf{a}_1$ and $\mathbf{a}_2$ forming an angle of 60°, and two atoms per primitive cell separated by the vector $\boldsymbol{\tau}$. Then we create two new supercell vectors $\mathbf{A}_1$ and $\mathbf{A}_2$ by means of the matrix M according to $\mathbf{A}_i = \sum_j M_{ij}\mathbf{a}_j$. The supercell itself is also hexagonal if

$$\mathrm{M} = \begin{bmatrix} p & q \\ -q & p+q \end{bmatrix} \tag{1}$$

with p and q integers. We will name it the "(p, q) supercell". We can construct a first kind of moiré bilayer by placing a (p, q) cell above its mirrored image (q, p). The angle of misorientation (twist angle) is fixed by the $\{q, p\}$ pair according to the formula:

$$\tan\theta = \sqrt{3}\frac{p^2 - q^2}{p^2 + q^2 + 4pq}\,. \tag{2}$$

A second kind of structures exists, based on a similar coincidence. The application of a $\pi/3$ rotation on the (p, q) supercell vectors $\mathbf{A}_i$ is equivalent to construct them from the basis $\{\mathbf{a}_2, \mathbf{a}_2 - \mathbf{a}_1\}$ instead of $\{\mathbf{a}_1, \mathbf{a}_2\}$. The corresponding matrix writes:

$$\mathrm{M}' = \begin{bmatrix} -q & p+q \\ -p-q & p \end{bmatrix}\,. \tag{3}$$

Let us call this "$(-q, p+q)$ supercell". It spans the same area as the previous (p, q) supercell, but the atomic disposition inside it is different. Now, placing this $(-q, p+q)$ supercell over the (q, p) one leads to a different twist angle defined by

$$\tan\theta' = \sqrt{3}\frac{q^2 + 2pq}{2p^2 - q^2 + 2pq}\,. \tag{4}$$

The three supercells defined above and the resulting angles θ and θ' are sketched in Figure 1.a. The p and q integers obey to some constraints however: they must be different and non zero, they must have no common divisor, and the cases $p - q$ multiple of 3 have to be excluded as they correspond to angles of 0° and 60°, or to non primitive moiré supercells. However, the nomenclature introduced here for twisted bilayers can be employed also for untwisted structures by considering the $(0, 1)$ case. Moreover, since the angles (2) and (4) are defined modulo 60°, the definitions (1) and (3) are not unique. In order to establish a non ambiguous set of structures we will impose arbitrarily $p > q > 0$ implying that both θ and θ' are positive and $\theta + \theta' = 60°$.

Designing moiré bilayer hexagonal structures requires then two integers p and q, as well as the respective positions of layers. Let us introduce the notation $(p, q)_X$, X being the origin of the supercell. It can be either a boron B ("A" sublattice), a nitrogen N ("B" sublattice) or an hexagon H. The origin of the lower layer is arbitrarily located on a site of the "A" sublattice (i.e. a boron atom in case of hBN) and its supercell is accordingly labeled $(q, p)_B$. The upper layer supercell is either based on the $(p, q)_X$ or on the $(-q, p+q)_X$ construction, with $X = B$, N or H. As a consequence, one ends up with six bilayers that can be identified by the supercell indexes p and q and the origin of the upper layer X. The construction is sketched in Figure 1 where we report the example of the $(1, 2)_B$ supercell for the lower layer (panel b) and either the $(2, 1)_X$ supercells (in blue) or the $(-2, 3)_X$ ones (in yellow) for the upper layer (panels c-e), with $X = B$, N or H. The six stacking geometries are listed in Table I. Note that in Table I angles appear with a sign. It is worth stressing that this sign is actually meaningful because moiré bilayer honecomb systems are chiral structures. We hence define the sign of the twist angle as the screw angle separating BN bonds at the atom-on-

upper layer	angle	group	stacking	double SC
$(p,q)_B$	$+\theta$	$p321$	**BB**	no
$(p,q)_N$	$-\theta'$	$p321$	**BNNB**	yes
$(p,q)_H$	$+\theta$	$p321$	**NN**	no
$(-q,p+q)_B$	$-\theta'$	$p312$	**BBNN**	yes
$(-q,p+q)_N$	$+\theta$	$p3$	**BN**	no
$(-q,p+q)_H$	$+\theta$	$p3$	**BN**	no

TABLE I. Overview table summarizing the geometry of the five stackings of hBN twisted bilayers. The lower layer is based on the $(q,p)_B$ supercell.

atom coincidence sites of the supercell, as depicted in the insets of the Figure 2.

Depending on the coincident atoms, one can distinguish between (i) two geometries with a *double* sublattice coincidence per cell, the $(p,q)_N$ and the $(-q,p+q)_B$, and with an angle of twist $-\theta'$ defined by equation (4) and (ii) four geometries with a *single* sublattice coincidence per cell, $(p,q)_B$, $(p,q)_H$, $(-q,p+q)_N$ and $(-q,p+q)_H$, with an angle of twist θ defined by equation (2). It is trivial however to remark that the latter two are related by a simple inversion and are therefore identical. All this boils down to five hexagonal stackings for the generic twisted hBN bilayer. While (q,p) identifies the supercell, and is therefore related to the moiré periodicity and angles, we will adopt the notation BBNN, BNNB, BB, BN and NN to identify the five hexagonal stacking of the generic supercell, inspired by the coincident atoms between the two layers. Images of these stackings, their layer symmetry group ($p3$, $p321$ or $p312$) and the transformations to be applied to switch from one stacking to another (swapping of B/N atoms in one layer or translation by $\pm\boldsymbol{\tau}$) are summarized in Figure 2 and Table I.

For comparison, in the case of graphene bilayers both A and B sublattices vertces are carbon atoms and there is no need to explore the different origins of the supercell (both start from "A" sublattice). It results that only two stacking sequences are possible. The first is related to equations (1) and (2), it belongs to the $p321$ layer group and to the *odd* bilayer graphene (BLG) set [24, 30–32], has a *single* sublattice vertical coincidence per cell and the twist angle is θ. The second graphene bilayer is related to equations (3) and 4, it belongs to the $p622$ layer group and to the *even* BLG set with hexagon-hexagon or *double sublattice* coincidence. Its rotation angle is $-\theta'$.

At last, remembering that the twisted bilayers are chiral structures, if we swap the value of p and q we obtain five new stackings, based on the (p,q) lower layer supercell. They are exactly the mirror images of the five (q,p) structures with the same electronic structure and with the twist angles $+\theta'$ for the BNNB and BBNN and $-\theta$ for the BB, BN and NN stackings. Complete definitions and demonstrations are given in the Supplemental Materials.

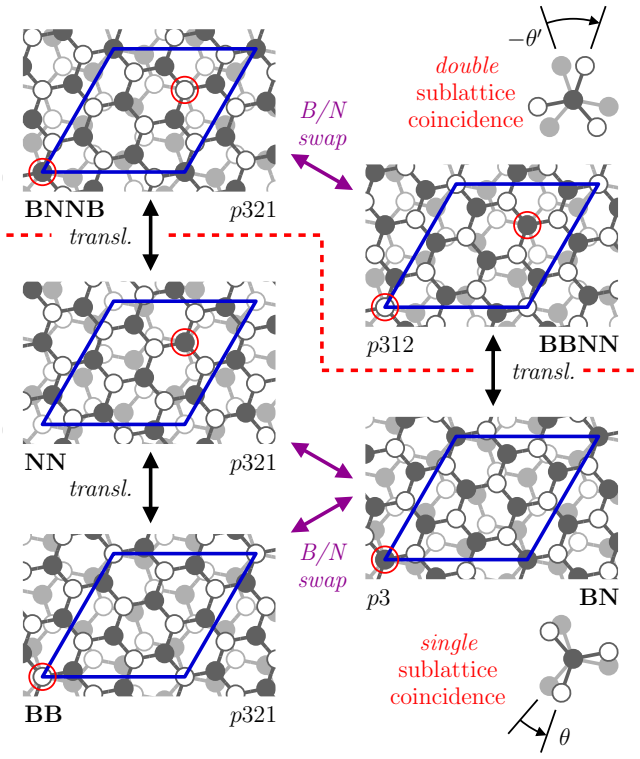

FIG. 2. The five stackings of hBN moiré structures, with $p=2$ and $q=1$. The sublattice coincidences are highlighted with red circles.

Based on our robust symmetry analysis, five different stackings are thus clearly identified in the case of BN bilayers whereas only two of them have been so far considered in litterature (i.e. NN and BN [23]). For these two, very specific electronic properties have been reported, demonstrating that a complete study involving all the stackings is mandatory.

Now that we have identified all stacking possibilities and established an unambiguous nomenclature to distinguish them, we can study how the stacking sequence modifies the band structure at fixed supercell. To this aim we have performed first-principle simulations in the density functional theory (DFT) framework in the generalised gradient approximation [33]. All the calculation parameters and the procedure to determine the equilibrium interlayer distance of the bilayers can be found in the Supplemental Materials. In a previous work [28] we highlighted that interlayer coupling is crucial in the formation of the indirect band gap of the bulk phase.In this context, particular care has been taken to obtain accurate results at the gap level. As a first step, the structural stabilities of the five principal untwisted bilayers are investigated highlighting two main groups (see Figure 10 of the Supplemental Materials). Indeed, the three most stable structures (BN(0,1), BNNB(0,1) and BB(0,1)) have a smaller equilibrium interlayer distance, whereas the two least stable ones (BBNN(0,1) and NN(0,1)) are around

Structure	Top valence		Bottom conduction	
	@M	@K	@M	@K
BNNB(1,2)	83	-	25	-
BN(1,2)	61	-	104	-
NN(1,2)	148	20	178	-
BB(1,2)	38	-	232	110
BBNN(1,2)	163	20	273	110

TABLE II. The band splitting (meV) at M and K in the top valence and bottom conduction of the (1,2) supercells. The symbol '-' indicates a band crossing. These features are highlighted with red vertical lines in figure 3.

10 meV per formula unit higher in energy and have a larger equilibrium interlayer distance. Regarding the electronic properties, untwisted bilayers with a boron-on-boron conicidence (BBNN(0,1) and BB(0,1)) have an indirect band gap whereas the other structures have an indirect gap. More details about the untwisted bilayers can be found in the Supplemental Materials.

We now focus on twisted bilayers and we adopt the $(1, 2)$ configuration for all stackings because of computational convenience and because notable effects are more distinguishable. The nomenclature we adopted has the advantage of immediately telling what atomic species are on top of each other and this characteristic has clear signatures in the band structure. The DFT results are reported in Figure 3. Note that the momentum path is traced inside the bilayer supercell. It is important to recall that the preservation of the hexagonal symmetry of the supercell implies the conservation of their order-3 rotation axes without which the moiré superstructure is not hexagonal and the equivalence between the K points of the Brillouin zone is broken. Interestingly, our calculations reveal that the gap is always indirect whatever the stacking with a constant value around 4.3 eV (see Table.III). By analyzing in details the electronic structure, we can distinguish the stackings according to their behavior at the K and M points. In the valence region we observe that when N atoms are on top of each other (the NN and the BBNN stackings), a band crossing is avoided in the top valence at K while the splitting between the HOMO and HOMO-1 at M is the largest. On the conduction band, the splitting between the LUMO and the LUMO+1 at M is reduced along the sequence BBNN, BB, NN, BN and BNNB while the presence of B atoms on top of each other (BB and BBNN stackings) prevents a band crossing at K otherwise clearly observable in the other bilayers. All the features discussed here are highlighted with dashed vertical red lines in Figure 3 and reported in Table II. We expect these effects to be less important at small twist angles because the immediate surroundings of each atom change more progressively than at large twist angles.

We can now pass to the investigation of the evolution of

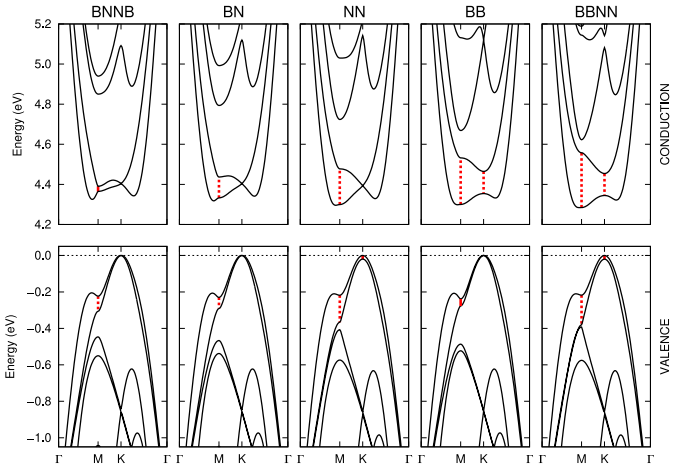

FIG. 3. Bottom conduction and top valence of the five principal stackings in the $(1, 2)$ supercell. Red vertical dashed lines highlight the notable splittings at M and K in the top valence and bottom conduction regions. Their values are reported in Table II.

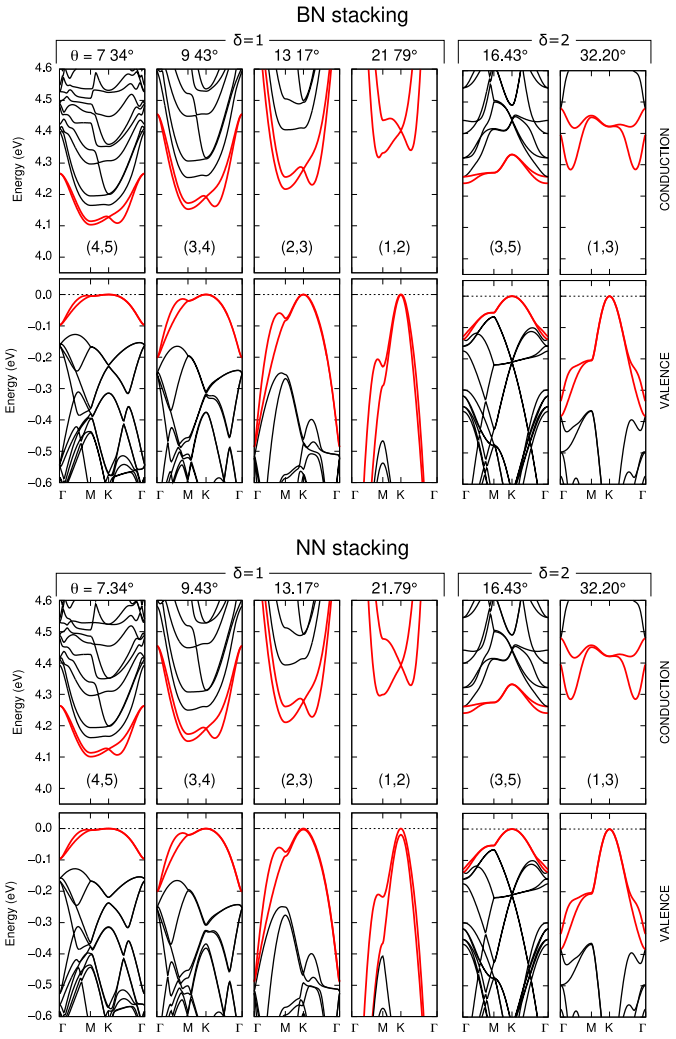

FIG. 4. Bottom conduction and top valence of the BN and NN stackings at different twist angles.

family	supercell	BNNB	BN	NN	BB	BBNN
$\delta = 1$	(1,2)	4.325 (71)	4.318 (76)	4.296 (88)	4.299 (55)	4.284 (60)
	(2,3)	4.221 (30)	4.217 (34)	4.211 (38)	4.203 (41)	4.202 (42)
	(3,4)	4.153 (15)	4.153 (16)	4.151 (17)	4.145 (18)	4.146 (19)
	(4,5)	4.102 (5)	4.103 (5)	4.101 (5)	4.098 (5)	4.099 (5)
$\delta = 2$	(1,3)	4.284 (137)	4.284 (137)	4.284 (137)	4.284 (136)	4.284 (136)
	(3,5)	4.240 (72)	4.241 (72)	4.240 (72)	4.240 (72)	4.241 (72)

TABLE III. Energy gap (eV) of the indirect band gap at different twist angles and stacking sequences. In parenthesis: energy difference between the direct and the indirect band gap in meV.

the band structure as a function of the twist angle. More precisely, we calculated the band structure of thirty BN bilayers corresponding to six twist angles (i.e. six (p,q) pairs) for each of the five hexagonal stackings. In the main text we discuss two paradigmatic stackings, the BN and the NN one and we report the corresponding twelve band structure plots in Figure 4. We refer the reader to the Supplemental Materials for the other structures.

First, we observe that the gap varies strongly with the twist angles. More precisely, it gets smaller (higher) for smaller θ (θ'), demonstrating a trend opposite to what predicted by continuous models [22]. Typically, for θ varying from 21.79° to 7.34°, the gap decreases significantly by ∼5%. Secondly, we observe that the gap remains indirect irrespective of the angle in all stackings. This finding contrasts with less accurate calculations based on density-functional tight-binding method where a direct gap is obtained at all twist angles [23]. Lastly, conduction and valence bands get flatter at smaller angles as seen in Figure 4. For example, in the BN stacking at θ =7.34°, the HOMO and LUMO states are characterized by bandwidths around 0.09 eV and 0.16 eV, respectively. A complete analysis detailed in the Supplemental Materials allows us to affirm that it is not an artifact coming from σ or nearly-free-electron states located at higher energies. Consequently, two localized states tend to arise in the gap for small angles. Obviously, the presence of very flat bands is not observed since it would require to consider much smaller angles. As a result, our calculations show that by reducing the twist angle it may be possible to tune/reduce the difference between indirect and direct gap, hence convert progressively the radiative decay pathway from a phonon-assisted emission to a direct recombination. This may have strong impact on the intensity of emitted light (probability of recombination), its temperature dependence (through the coupling with phonons) and finally the life time of excitations. At this point we should stress that these results are reliable as long as one considers energy differences and trends. In fact, quasiparticle corrections, included for instance via the GW approximation, will not change significantly form one system to the other and have minor effect on the dispersion of s and p states.

In addition we noted that (p, q) configurations can be grouped in families defined by the parameter $\delta = |p - q|$ that characterizes the interplay between crystalline structure (twist angle) and electronic structure (bands). In fact, the bands around the gap within the same family look similar but shrunk and flattened at smaller angles. Consider, for example, the first four plots from the left in the band plots of Figure 4, which belong to the family $\delta = 1$. Here the valence band present a maximum in K and is formed by two bands dispersing almost parabolically, up to the M point where one of the two exhibits a small bump. In conduction, two valleys are well discernible around M and between K and Γ, the former constituting the conduction band minimum. The last two plots from the left in the band plots of Figure 4 belong to the $\delta = 2$ family. Characteristics of the conduction and valence are very different from the other family, even though the gap remains indirect with the top valence at K. However, as before, one can identify similar features within the same family that remain unchanged

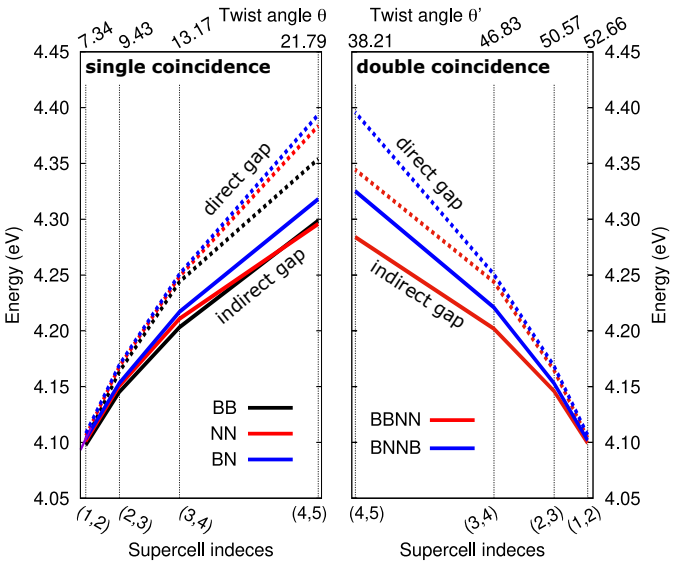

FIG. 5. Indirect gap (solid lines) and lowest direct transition (dashed lines) of the five stackings as a function of the twist angle (θ or θ' depending on the stacking) within the $\delta = 1$ family.

despite the band shrinking. This is quite evident for the valence band, with a characteristic double-dome shape (with a dome on top of another) and a maximum in K. In the conduction band, similarities are less evident, but one can see that the two bottom bands almost coincide in the $M-K$ line and present two minima much closer to Γ than in the $\delta=1$ family. We verified that the bottom conduction in the $\delta=2$ does fall in the $\Gamma-M$ high symmetry line (see Supplemental Materials). The DFT values of the indirect band gap and the difference between direct and indirect gap for both families in the six considered supercells are reported in Table III.

To conclude, we have demonstrated that, at variance from graphene bilayers, in BN bilayers there are more possibile stackings at a given moiré periodicity. We have demonstrated that there are only five stackings that are invariant under rotations of 120° as the pristine BN monolayers. We have listed the symmetry groups of these stackings, shown how to construct them and how to transform one into another and we have introduced a physically informative nomenclature allowing to identify them unambiguously and define precisely the twist angle (θ or θ' depending on the stacking). Moreover this nomenclature is completely general and can be applied to any homobilayer formed of hexagonal 2D materials (twisted as well as untwisted). By performing DFT simulations at the GGA level, we have done a thorough study of the electronic structure of BN bilayers taking into account both its dependence on the stacking sequence and the twist angle. In the first case, we have traced a correlation between the B-on-top-of-B or N-on-top-of-N coincidences and some features of the band structure in the top valence and bottom conduction regions. In the second case, we have shown that the gapwidth is always indirect irrespective of the twist angle and it decreases for decreasing θ or for increasing θ', differently from what previously predicted on the basis of less sophisticated theoretical models.[22] . Finally we have identified the geometrical parameter $\delta=|p-q|$ which allows to classify bilayers into families with similar band structures. The stacking- and angle-dependent properties discussed in this letter are expected to have a strong impact on the optical properties of such bilayers and in particular on the direct manipulation of interlayer excitons which can be stabilized through the application of an external field.

SUPPLEMENTAL MATERIALS

Asymetric honeycomb supercells

The boron nitride moiré structures are 2D periodic structures based on honeycomb networks. We choose the two primitive vectors $\mathbf{a}_1=a(\sqrt{3}/2,-1/2)$ and $\mathbf{a}_2=a(\sqrt{3}/2,1/2)$ with an angle of 60° and define the three

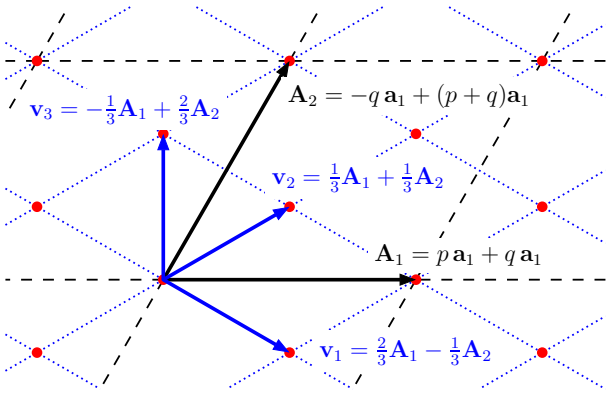

FIG. 6. The upper layer asymmetric supercell (p,q) with $p=q+3t$. It is always possible to construct a smaller supercell since $\mathbf{v}_1$, $\mathbf{v}_2$ and $\mathbf{v}_3$ are vectors of the honeycomb lattice. In other words, the twisted bilayer geometries made from the $(q,q+3t)$ supercell are not primitive cells of the moire.

vectors separating the B and the A sublattices like:

$$\boldsymbol{\tau}_1=+\mathbf{a}_1/3+\mathbf{a}_2/3 \qquad \boldsymbol{\tau}_2=\boldsymbol{\tau}_1-\mathbf{a}_1 \qquad \boldsymbol{\tau}_3=\boldsymbol{\tau}_1-\mathbf{a}_2 \quad (5)$$

The new periodic super-lattice is constructed with the new transnational vectors $\mathbf{A}_1$ and $\mathbf{A}_2$ written on the base $\{\mathbf{a}_1,\mathbf{a}_2\}$ like $\mathbf{A}_i=\sum_j M_{ij}\mathbf{a}_j$. The supercell is hexagonal if and only if its matrix can be written like

$$\mathrm{M}_{\mathrm{lower}}=\begin{bmatrix} m & n \\ -n & m+n \end{bmatrix} \quad (6)$$

with n and m integers, and vertical mirror planes along high symmetry directions of the supercell are lost only if

$$m,n\neq 0 \text{ and } m\neq n$$

and the supercell is *asymmetric*.

The asymmetric supercells belong th the 2D layer group $p\bar{6}$ (obviously, the internal translation are neglected). This group contains three axes of improper rotations $\bar{6}$ selon z respectively located in $(0\,0)$, $(\frac{1}{3}\,\frac{1}{3})$ and $(\frac{2}{3}\,\frac{2}{3})$ highlighted with red dots in Figure 6.

Lastly, the m and n integers define also the parameter length, the surface and the numer of atoms of the the supercell

$$\begin{aligned} |\mathbf{A}_i| &= a\sqrt{m^2+n^2+mn} \\ \Omega &= \Omega_0\left(m^2+n^2+mn\right) \\ \mathrm{N}_{\mathrm{at}} &= 2\left(m^2+n^2+mn\right) \end{aligned} \quad (7)$$

with $\Omega_0=\frac{a^2\sqrt{3}}{2}$ is the surface, and a is the cell parameter of the honeycomb primitive cell.

Why the case $(p-q=3t)$ is useless?

The case $\alpha=0$ corresponds to moiré supercells where $p-q=3t$. As we sketched in figure 6, starting from the

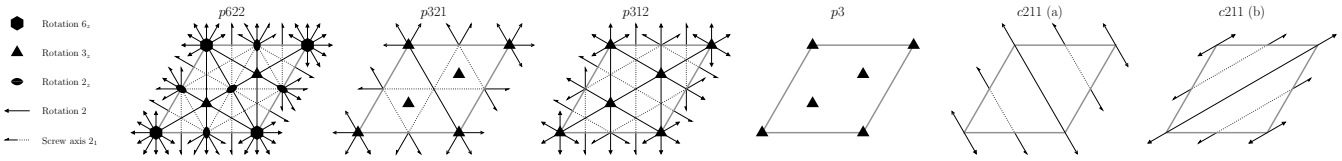

FIG. 7. All the possible layer groups of the moire bilayer graphene and h-BN periodic structures (adapted from [34], see text). The trivial group $p1$ is not shown.

(p, q) supercell vectors $\mathbf{A}_1$ and $\mathbf{A}_2$, we can define new shorter vectors

$$\mathbf{v}_1 = \frac{2}{3}\mathbf{A}_1 - \frac{1}{3}\mathbf{A}_2 = (q + 2t)\,\mathbf{a}_1 - t\,\mathbf{a}_2 \quad (8)$$

$$\mathbf{v}_2 = \frac{1}{3}\mathbf{A}_1 + \frac{1}{3}\mathbf{A}_2 = t\,\mathbf{a}_1 + (q + t)\,\mathbf{a}_2 \quad (9)$$

$$\mathbf{v}_3 = -\frac{1}{3}\mathbf{A}_1 + \frac{2}{3}\mathbf{A}_2 = (-q - t)\,\mathbf{a}_1 + (q + 2t)\,\mathbf{a}_2 \quad (10)$$

and since q and t are integers, the vectors $\mathbf{v}_i$ are honeycomb bravais lattice vectors.

Moreover, when $p = q + 3t$ the equations of the twis tangles read

$$\tan\theta = \sqrt{3}\frac{3t^2 + 2qt}{2q^2 + 3t^2 + 6qt}$$

$$\tan\theta' = \sqrt{3}\frac{q^2 + 2qt}{q^2 + 6t^2 + 6qt}$$

Layer groups of moiré structures

The layer group of a graphene monolayer asymmetric supercell is the $p6/m$, neglecting translations occurring inside the defined cell. For a boron nitride (or a transition metal dichalcogenide) supercell, the layer group is $p\bar{6}$ [34]. All the symmetry groups graphical representations are sketched in the figure 7.

When stacking two supercells as described above, the 3 rotation axes are always preserved. In the case of pure graphene bilayers, the $(-q, p + q)$-on-(q, p) structure geometry has a *double* sublattice coincidence and an "hexagon-hexagon" 6-order rotation axis (in addition to two 3-order axis). Its layer group is $p622$. The case of (p, q)-on-(q, p) structure corresponds to the *single* sublattice coincidence and two "hexagon-atom". It contains three 3-order rotation axes. The group is $p321$ for this case.

Hexagonal BN monolayer has a smaller symmetry group than graphene.

At last, the lowest symmetry situation occurs when stacking a (p, q) or a $(-q, p + q)$ supercell on a (q, p) cell with a totally random translation. All the point symmetry operations are lost, the crystal system is *oblique*, the layer group is the simplest $p1$ and only the $+\mathbf{k}/-\mathbf{k}$ symmetry is conserved in the reciprocal plane (hence, the three point K, K′ and K″ are nonequivalent)

Computational details

Calculations have been done with the free simulation packages Quantum ESPRESSO [35, 36] (band structure of twisted bilayers) and ABINIT [37, 38] (stability of twisted and untwisted bilayers).

In both cases norm-conserving pseudopotentials have been used. We checked that changing from one software to the other was not introducing major errors in the main characteristics discussed in the paper. In both groups of calculations, the cutoff energy was 30 Ha and we sampled the Brillouin zone with a Monkorst-Pack grid of $5 \times 5 \times 1$ k-points in all supercells ($9 \times 9 \times 1$ in the untwisted cases). The equilibrium interlayer distance has been fixed at 3.22 Å in all bilayers as detailed below. The in-plane cell parameter was $a = 2.23$ Å and no in-plane relaxation has been done. A cell height L =15 Å has been used in all calculations unless specified differently. This value has

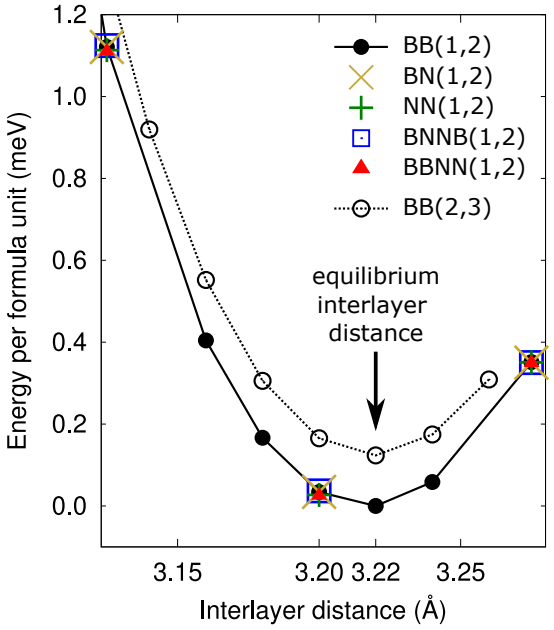

FIG. 8. Total energy calculation of the five stackings in the (1,2) supercell as a function of the interlayer distance h. The BB(1,2) is the full black line with black bullets and the BB(2,3) is the dotted line with empty circles. The other (1,2) stackings are superimposed to the BB(1,2) curve almost exactly and are reported with different colors and symbols.

been fixed by paying attention to the alignment of the σ and π conduction bands. In fact, as already pointed out by several authors [15, 39–44] the bottom conduction in Γ is composed of nearly-free-electron (NFE) states that extend for several Ångströms above the layer and thus converge very slowly with the amount of vacuum (see the dedicated Appendix for more details).

Stability and interlayer distance

To fix the interlayer distance, we calculated the total energy per unit formula $E(h)$ at different input values of the interlayer distance h. Results are reported in Figure 8 and summarized in Table IV. We took the BB(1,2) and the BB(2,3) bilayers as reference structures. For these bilayers, we sampled h on a fine grid. Both bilayers have the energy minimum at $h = 3.22$ Å, with a negligible energy difference (~ 0.1 meV per formula unit). Then we computed $E(h)$ for the BN(1,2), NN(1,2), BNNB(1,2) and BBNN(1,2) bilayers on a coarser grid and found that the points fell basically on top of the BB(1,2) curve. Following this analysis, we assumed that we can safely fix the equilibrium distance at $h = 3.22$ Å irrespective of the stacking or the twist angle. We note however that this value may be inaccurate for very small twist angles that are not investigated in this work.

Untwisted bilayers

It is possible to extend the nomenclature we introduced in the main text also for untwisted bilayers. In this case, only the stacking label is meaningful, the (q, p) pair being trivially 1 and 0 (see Figure 10).

In Figure 10 we report an image of the structure of the five untwisted stackings and their stability curve $E(h)$ together with that of the BB(1,2) bilayer. We observe that the three most stable untwisted structures, i.e. the BN(0,1), the BNNB(0,1) and the BB(0,1) have a smaller equilibrium distance, whereas for the two most unstable, the NN(0,1) and the BBNN(0,1), the equilibrium h is larger, so that the twisted bilayers falls somewhat between the two groups. This makes sense if one reckon that inside the same twisted bilayer one can find domains with a local stacking intermediate to the five untwisted ones.

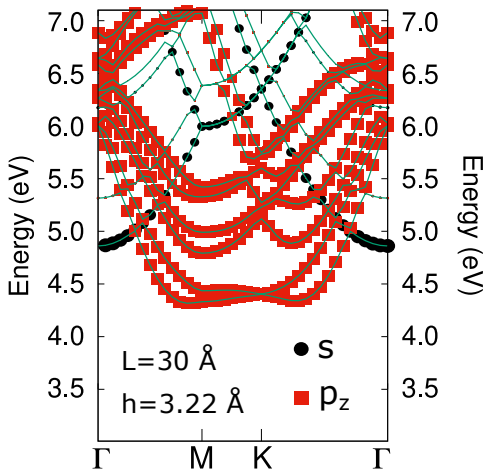

FIG. 9. Orbital momentum component of the conduction bands conduction bands of the BN(1,2) bilayer (fat bands)

In experiments it is observed that, far from certain angles, it is pretty easy to move or twist a BN flake on top of another, and this is consistent with the negligible energy differences we calculated between different stackings at fixed angle and between the two reference calculations with the same stacking sequence. However when the twist angle gets close to some specific values, the flake gets stuck and no further twist is possible. In fact, the large energy differences with the untwisted configurations (order of 10 meV per unit formula) suggest that when approaching small twist angles the bilayer falls into one of the energetically more favorable configurations, possibly undergoing large in-plane deformation to maximize the size of the untwisted domains. [21, 45–47].

The equilibrium distances, the total energy per BN pair with respect to the BB(1,2) bilayer and the values of the DFT direct (at K) and indirect band gaps (between valleys close to K and the point M) are reported in Table IV.

System	h (Å)	$E_{\rm BN}$ (meV)	$E_{\rm ind}$ (eV)	$E_{\rm dir}$ (eV)
BBNN(0,1)	3.425	8.7	3.957	4.037
NN(0,1)	3.375	6.8	4.345	4.037
BB(2,3)	3.220	0.1	4.217	4.251
BB(1,2)	**3.220**	**0**	**4.318**	**4.394**
BB(0,1)	3.150	-8.3	3.950	4.436
BNNB(0,1)	3.125	-11.1	4.649	4.398
BN(0,1)	3.100	-12.8	4.463	4.438

TABLE IV. Equilibrium interlayer distance h, total energy per formula unit $E_{\rm BN}$ with respect to the (1,2) bilayers, smallest indirect gap $E_{\rm ind}$ (eV) and energy of the smallest direct transition $E_{\rm dir}$ (eV) (direct gap).

Nearly-free-electron states

As already pointed out by Blase and coworkers in the case of bulk hBN [15], the conduction states at Γ converge very slowly with the amount of vacuum because they correspond to some unoccupied N-centered nearly-free-electron (NFE) state extending for several Ångströms above the BN layer [15, 39–44]. These NFE states have a neat $3s$ orbital component, as shown in the fat-band plot reported in Figure 9.

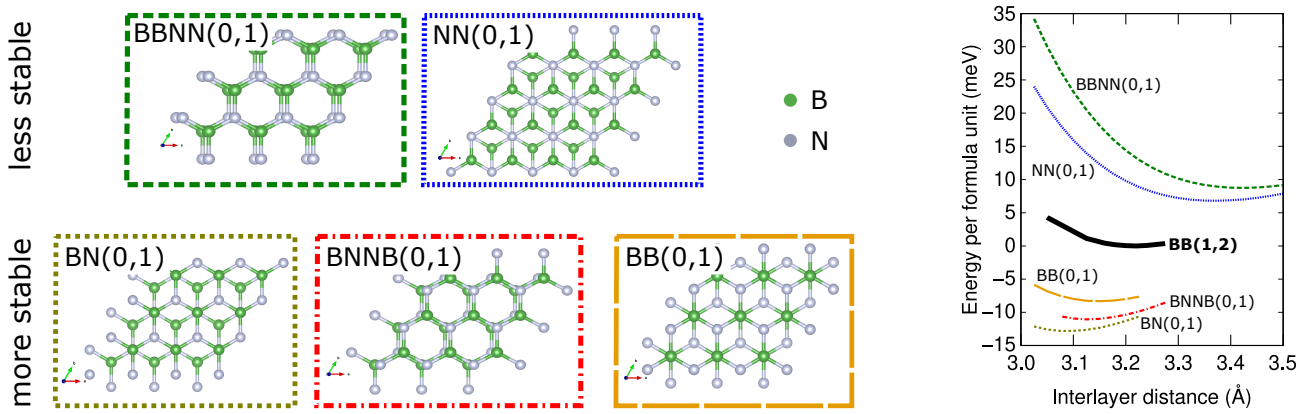

FIG. 10. The five hexagonal stackings in untwisted bilayers and their stability curves with respect to the BB(1,2) twisted bilayer (thick black solid line).

Their alignment with respect to the π bands is a delicate issue on the purpose of this article because the energy difference between the bottom of the unoccupied σ band and the bottom of the unoccupied π band are very close in energy and they may compete in determining the indirect nature of the gap. Therefore, it is worth paying much attention to their convergence. To this aim, we made a series of two test calculations in a BN(1,2) bilayer. First we tested the evolution of these states as a function of the height of the simulation cell at fixed interlayer distance (the three panels of Figure 11a). This test shows that by reducing the cell height, these states are pushed toward higher energies because of fictitious cell-to-cell interactions. Replicas of the system must be separated of around $L \sim 20$ Å for the band dispersion and alignment to be converged. Note that we decided on purpose to carry out our simulations with a slightly lower value (15 Å) because the fact of pushing the NFE states to higher energies is not detrimental to our investigation and allows us to reduce the computational workload.

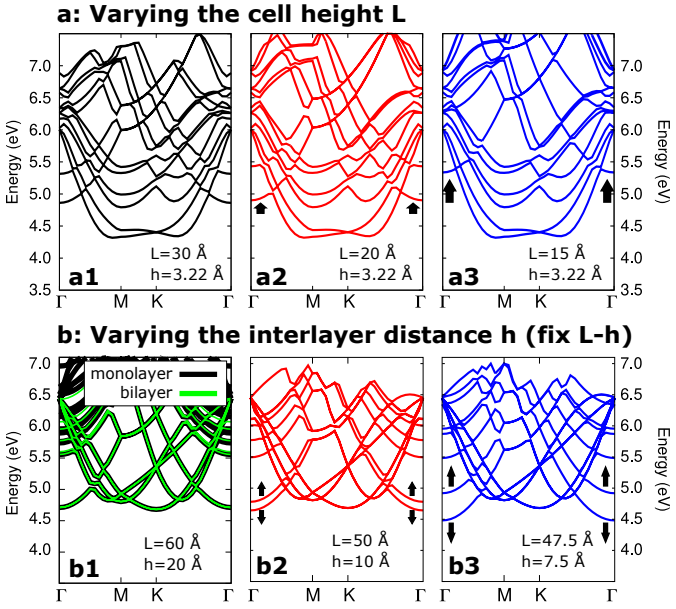

FIG. 11. The evolution of the NFE states as a function of the simulation parameters in the BN(1,2) bilayer. **a**: evolution as a function of the cell height L at fixed interlayer dsitance ($h = 3.22$ Å). $L = 30$, 20 and 15 Å in panels **a1**, **a2** and **a3** respectively. **b**: evolution as a function of the interlayer dsitance h at fixed vacuum ($L - h = 40$ Å). $h = 20$, 10 and 7.5 Å in panels **c1**, **c2** and **c3** respectively. In panel **b1**, the band structure of the BN(1,2) bilayer (flashy green) is compared with that of the isolated monolayer (black).

Then we tested the evolution of the NFE state as a function of the interlayer distance leaving a constant amount of vacuum ($L - h$) of 40 Å, which is largely enough to prevent cell-to-cell interactions. In the panels of Figure 11b, we report three calculations of the BN(1,2) bilayer with a varying interlayer distance (20, 10 and 7.5 Å respectively in panels b1, b2 and b3). In the b1 panel, we also plot in black the conduction band of the isolated monolayer in the (1,2) supercell and we notice that it coincides with the $h = 20$ bilayer calculation. This test demonstrates that moving two layers closer to each other induces a bonding/antibonding splitting of the NFE states which increases as the layers get closer.

Since there is no difference between the interlayer distance separating two layers inside the cell and the space separating replicas of the simulated system, one should pay attention that these two effects (pushing to higher energies and band splitting) happen at the same time.

Gap crossover from the monolayer to the bilayer

In a previous article,[28] some of us showed that the interlayer coupling is crucial in the formation of the indirect band gap of the bulk phase. To check it also in the bilayer, we calculated the band structure of the BN(1,2) bilayer for h varying in the range between 10 Å and 3.22 Å within supercells of height $L = 30$ Å. Results

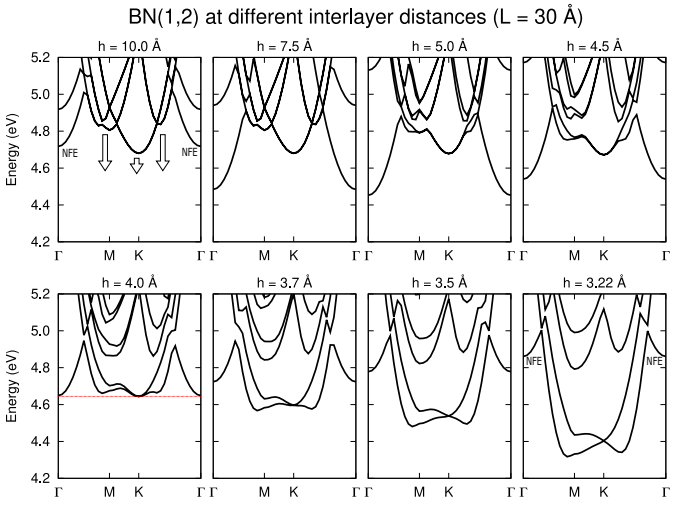

FIG. 12. Bottom conduction bands of a BN(1,2) supercell at different values of the interlayer distance h ranging from 10 Å (top left) to the equilibrium distance 3.22 Å (bottom right). Arrows indicate how the π bands evolve when reducing the interlayer distance. The NFE bands are highlighted with a label. A dotted red line highlights the gap crossover (see text).

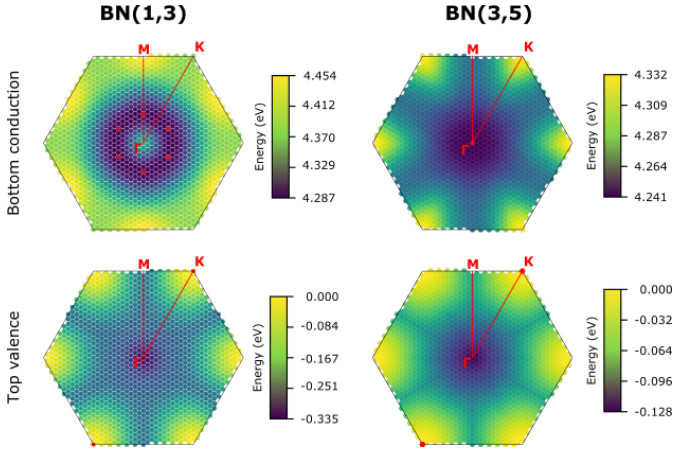

FIG. 13. Energy surface of the lowest empty band (top panels) and the highest occupied band (bottom panels) of the BN(1,3) and the BN(3,5) bilayers from left to right. The top valence and the bottom conduction states are highlighted with red hexagons.

are reported in Figure 12.

We found that in all calculations the top valence was at K (not shown). At the equilibrium interlayer distance (h=3.22 Å), an indirect band gap is formed between the top valence at K and a point close to M. At variance, in the monolayer limit ($h = 10$ Å), the gap is direct with a bottom conduction at K as predicted by several theoretical studies.[15, 16, 28, 44, 48–52] Please, note that the band structure looks quite different from the plots published elsewhere, because we worked with a (1,2) supercell even in the monolayer limit. Besides the valley in K, two other valleys can be distinguished: one at around M and another at approximately 30% of the $K-\Gamma$ line (above the long arrows in the Figure 12). All these states have a π (p_z) orbital character. As h gets smaller, these two side valleys go down in energy faster than the levels at K, and eventually end up forming the bottom conduction at the equilibrium interlayer distance.

On the other hand, for h below the monolayer limit but still large (10 Å$< h <$ 4 Å), the actual bottom conduction is at Γ. This is due to the interaction between nearly-free-electron (NFE) states with the s orbital character [15, 39–44] floating above the surfaces of the BN layers. These states move globally upward when the distance between two layers is reduced, but at the same time the bonding/antibonding splitting due to their interaction increases violently, pushing the NFE contribution to low energies. The result of this competition is that for large h (between 20 Å and 7.5 Å), the bonding states move to low energy and constitute the bottom of the conduction band, but for $h <$ 7.5 Å, they retract and move back to higher energy. At around h =4 Å, there is a gap crossover highlighted by a red dotted line in the corresponding panel. At this interlayer distance, the π side valleys gets to lower energies than the rest of the conduction band giving origin to the indirect band gap of the equilibrium configuration. Details on the orbital character of the conduction band and the delicate convergence of the NFE states have been discussed on a previous Appendix.

These simulations suggest that it may be possible to control the nature of the bandgap by intercalation ($K \to M$, or $K \to K$ for $\pi \to \pi$ transitions, or $K \to \Gamma$ for $\pi \to \sigma$ transitions) and possibly take advantage from the competition between two indirect and one direct emission pathways.

Band gap of the $\delta = 2$ family

In the main text we give the values of the gapwidth of the five stackings of the (1,3) and (3,5) supercells. The values have been extracted from the corresponding band plots, so they refer to gapwidths calculated along specific high symmetry paths in the Brillouin zone. In this section we report a more complete mapping of the band structure of the top valence and bottom conduction of the BN stacking, chosen as representative of the bilayers. In Figure 13 we report the energy surface of the highest occupied states and the lowest unoccupied states in the BN(1,3) and BN(3,5) bilayers. With this analysis we demonstrate that the values reported in the main text are meaningful because the bottom of the conduction and the top of the valence fall indeed on the high symmetry lines.

For this analysis we acknowledge F. Paleari who kindly

provided us with a dedicated analysis post-processing tool.

Band structure of the other stackings

Here below we report the band plots missing in the main text corresponding to stackings $BBNN$, NN and $BNNB$.

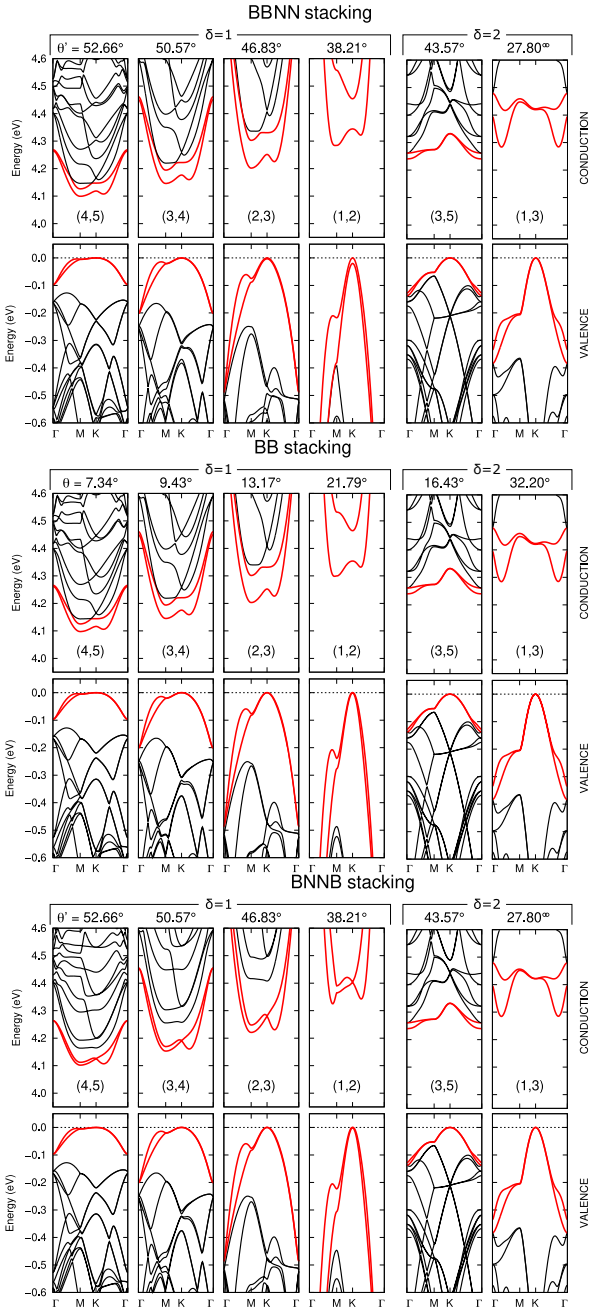

FIG. 14. Band structure as a function of the twist angle of the BBNN, BB and BNNB stackings from top to bottom.

[1] S. Carr, S. Fang, and E. Kaxiras, Nat. Rev. Mater. **5**, 748 (2020).

[2] E. Suárez Morell, J. D. Correa, P. Vargas, M. Pacheco, and Z. Barticevic, Phys. Rev. B **82**, 121407 (2010).

[3] R. Bistritzer and A. H. MacDonald, Proc. Natl Acad. Sci. **108**, 12233 (2011).

[4] L. Balents, C. R. Dean, D. K. Efetov, and A. F. Young, Nature Physics **16**, 725 (2020).

[5] D. M. Kennes, M. Claassen, L. Xian, A. Georges, A. J. Millis, J. Hone, C. R. Dean, D. N. Basov, A. N. Pasupathy, and A. Rubio, Nature Physics **17**, 155 (2021).

[6] B. Liu, L. Xian, H. Mu, G. Zhao, Z. Liu, A. Rubio, and Z. F. Wang, Phys. Rev. Lett. **126**, 066401 (2021).

[7] J. Choi, M. Florian, A. Steinhoff, D. Erben, K. Tran, D. S. Kim, L. Sun, J. Quan, R. Claassen, S. Majumder, J. A. Hollingsworth, T. Taniguchi, K. Watanabe, K. Ueno, A. Singh, G. Moody, F. Jahnke, and X. Li, Physical Review Letters **126**, 047401 (2021), arXiv:2007.15196.

[8] E. M. Alexeev, D. A. Ruiz-Tijerina, M. Danovich, M. J. Hamer, D. J. Terry, P. K. Nayak, S. Ahn, S. Pak, J. Lee, J. I. Sohn, M. R. Molas, M. Koperski, K. Watanabe, T. Taniguchi, K. S. Novoselov, R. V. Gorbachev, H. S. Shin, V. I. Fal'ko, and A. I. Tartakovskii, Nature **567**, 81 (2019), arXiv:1904.06214.

[9] C. Jin, E. C. Regan, A. Yan, M. Iqbal Bakti Utama, D. Wang, S. Zhao, Y. Qin, S. Yang, Z. Zheng, S. Shi, K. Watanabe, T. Taniguchi, S. Tongay, A. Zettl, and F. Wang, Nature **567**, 76 (2019), arXiv:1812.09815.

[10] K. L. Seyler, P. Rivera, H. Yu, N. P. Wilson, E. L. Ray, D. G. Mandrus, J. Yan, W. Yao, and X. Xu, Nature **567**, 66 (2019).

[11] K. Tran, G. Moody, F. Wu, X. Lu, J. Choi, K. Kim, A. Rai, D. A. Sanchez, J. Quan, A. Singh, J. Embley, A. Zepeda, M. Campbell, T. Autry, T. Taniguchi, K. Watanabe, N. Lu, S. K. Banerjee, K. L. Silverman, S. Kim, E. Tutuc, L. Yang, A. H. MacDonald, and X. Li, Nature **567**, 71 (2019).

[12] F. Wu, T. Lovorn, E. Tutuc, I. Martin, and A. H. MacDonald, Phys. Rev. Lett. **122**, 086402 (2019).

[13] D. A. Ruiz-Tijerina and V. I. Fal'ko, Phys. Rev. B **99**, 125424 (2019).

[14] H. Ochoa and A. Asenjo-Garcia, Phys. Rev. Lett. **125**, 037402 (2020).

[15] X. Blase, A. Rubio, S. G. Louie, and M. L. Cohen, Physical Review B **51**, 6868 (1995).

[16] T. Galvani, F. Paleari, H. P. C. Miranda, A. Molina-Sánchez, L. Wirtz, S. Latil, H. Amara, and F. Ducastelle, Phys. Rev. B **94**, 125303 (2016).

[17] L. Schué, L. Sponza, A. Plaud, H. Bensalah, K. Watanabe, T. Taniguchi, F. Ducastelle, A. Loiseau, and J. Barjon, Phys. Rev. Lett. **122**, 067401 (2019).

[18] A. Rousseau, L. Ren, A. Durand, P. Valvin, B. Gil, K. Watanabe, T. Taniguchi, B. Urbaszek, X. Marie, C. Robert, and G. Cassabois, Nano Letters **21**, 10133 (2021).

[19] F. Paleari, T. Galvani, H. Amara, F. Ducastelle, A. Molina-Sánchez, and L. Wirtz, 2D Materials **5**, 045017 (2018).

[20] K. Yasuda, X. Wang, K. Watanabe, T. Taniguchi, and P. Jarillo-Herrero, Science **372**, 1458 (2021),

arXiv:2010.06600.
[21] C. R. Woods, P. Ares, H. Nevison-Andrews, M. J. Holwill, R. Fabregas, F. Guinea, A. K. Geim, K. S. Novoselov, N. R. Walet, and L. Fumagalli, Nature Communications **12**, 347 (2021), arXiv:2010.06914.
[22] H. Y. Lee, M. M. Al Ezzi, N. Raghuvanshi, J. Y. Chung, K. Watanabe, T. Taniguchi, S. Garaj, S. Adam, and S. Gradečak, Nano Letters **21**, 2832 (2021), pMID: 33591206, https://doi.org/10.1021/acs.nanolett.0c04924.
[23] X.-j. Zhao, Y. Yang, D.-b. Zhang, and S.-h. Wei, Physical Review Letters **124**, 86401 (2020).
[24] G. Trambly de Laissardière, D. Mayou, and L. Magaud, Nano Lett. **10**, 804 (2010).
[25] L. Xian, D. M. Kennes, N. Tancogne-Dejean, M. Altarelli, and A. Rubio, Nano Letters **19**, 4934 (2019).
[26] X.-J. Zhao, Y. Yang, D.-B. Zhang, and S.-H. Wei, Phys. Rev. Materials **5**, 014007 (2021).
[27] L. Wirtz, A. Marini, and A. Rubio, Phys. Rev. Lett. **96**, 126104 (2006).
[28] L. Sponza, H. Amara, C. Attaccalite, S. Latil, T. Galvani, F. Paleari, L. Wirtz, and F. Ducastelle, Physical Review B **98**, 125206 (2018).
[29] J. C. G. Henriques, B. Amorim, R. M. Ribeiro, and N. M. R. Peres, Phys. Rev. B **105**, 115421 (2022).
[30] E. J. Mele, Phys. Rev. B **81**, 161405(R) (2010).
[31] G. Trambly De Laissardière, D. Mayou, and L. Magaud, Physical Review B - Condensed Matter and Materials Physics **86**, 125413 (2012), arXiv:1203.3144.
[32] S. Shallcross, S. Sharma, E. Kandelaki, and O. A. Pankratov, Phys. Rev. B **81**, 1 (2010).
[33] J. P. Perdew, K. Burke, and M. Ernzerhof, Phys. Rev. Lett. **77**, 3865 (1996).
[34] V. Kopský and D. B. Litvin, eds., *International Tables for Crystallography, Volume E: Subperiodic groups* (Kluwer, 2002).
[35] P. Giannozzi, S. Baroni, N. Bonini, M. Calandra, R. Car, C. Cavazzoni, D. Ceresoli, G. L. Chiarotti, M. Cococcioni, I. Dabo, A. D. Corso, S. de Gironcoli, S. Fabris, G. Fratesi, R. Gebauer, U. Gerstmann, C. Gougoussis, A. Kokalj, M. Lazzeri, L. Martin-Samos, N. Marzari, F. Mauri, R. Mazzarello, S. Paolini, A. Pasquarello, L. Paulatto, C. Sbraccia, S. Scandolo, G. Sclauzero, A. P. Seitsonen, A. Smogunov, P. Umari, and R. M. Wentzcovitch, Journal of Physics: Condensed Matter **21**, 395502 (2009).
[36] P. Giannozzi, O. Andreussi, T. Brumme, O. Bunau, M. B. Nardelli, M. Calandra, R. Car, C. Cavazzoni, D. Ceresoli, M. Cococcioni, N. Colonna, I. Carnimeo, A. D. Corso, S. de Gironcoli, P. Delugas, R. A. DiStasio, A. Ferretti, A. Floris, G. Fratesi, G. Fugallo, R. Gebauer, U. Gerstmann, F. Giustino, T. Gorni, J. Jia, M. Kawamura, H.-Y. Ko, A. Kokalj, E. Küçükbenli, M. Lazzeri, M. Marsili, N. Marzari, F. Mauri, N. L. Nguyen, H.-V. Nguyen, A. O. de-la Roza, L. Paulatto, S. Poncé, D. Rocca, R. Sabatini, B. Santra, M. Schlipf, A. P. Seitsonen, A. Smogunov, I. Timrov, T. Thonhauser, P. Umari, N. Vast, X. Wu, and S. Baroni, Journal of Physics: Condensed Matter **29**, 465901 (2017).
[37] X. Gonze, B. Amadon, G. Antonius, F. Arnardi, L. Baguet, J.-M. Beuken, J. Bieder, F. Bottin, J. Bouchet, E. Bousquet, N. Brouwer, F. Bruneval, G. Brunin, T. Cavignac, J.-B. Charraud, W. Chen, M. Côté, S. Cottenier, J. Denier, G. Geneste, P. Ghosez, M. Giantomassi, Y. Gillet, O. Gingras, D. R. Hamann, G. Hautier, X. He, N. Helbig, N. Holzwarth, Y. Jia, F. Jollet, W. Lafargue-Dit-Hauret, K. Lejaeghere, M. A. L. Marques, A. Martin, C. Martins, H. P. C. Miranda, F. Naccarato, K. Persson, G. Petretto, V. Planes, Y. Pouillon, S. Prokhorenko, F. Ricci, G.-M. Rignanese, A. H. Romero, M. M. Schmitt, M. Torrent, M. J. van Setten, B. V. Troeye, M. J. Verstraete, G. Zérah, and J. W. Zwanziger, Comput. Phys. Commun. **248**, 107042 (2020).
[38] A. H. Romero, D. C. Allan, B. Amadon, G. Antonius, T. Applencourt, L. Baguet, J. Bieder, F. Bottin, J. Bouchet, E. Bousquet, F. Bruneval, G. Brunin, D. Caliste, M. Côté, J. Denier, C. Dreyer, P. Ghosez, M. Giantomassi, Y. Gillet, O. Gingras, D. R. Hamann, G. Hautier, F. Jollet, G. Jomard, A. Martin, H. P. C. Miranda, F. Naccarato, G. Petretto, N. A. Pike, V. Planes, S. Prokhorenko, T. Rangel, F. Ricci, G.-M. Rignanese, M. Royo, M. Stengel, M. Torrent, M. J. van Setten, B. V. Troeye, M. J. Verstraete, J. Wiktor, J. W. Zwanziger, and X. Gonze, J. Chem. Phys. **152**, 124102 (2020).
[39] M. Posternak, A. Baldereschi, A. J. Freeman, E. Wimmer, and M. Weinert, Phys. Rev. Lett. **50**, 761 (1983).
[40] M. Posternak, A. Baldereschi, A. J. Freeman, and E. Wimmer, Phys. Rev. Lett. **52**, 863 (1984).
[41] X. Blase, L. X. Benedict, E. L. Shirley, and S. G. Louie, Phys. Rev. Lett. **72**, 1878 (1994).
[42] X. Blase, A. Rubio, S. G. Louie, and M. L. Cohen, Europhysics Letters (EPL) **28**, 335 (1994).
[43] S. Hu, J. Zhao, Y. Jin, J. Yang, H. Petek, and J. G. Hou, Nano Letters **10**, 4830 (2010), pMID: 21049977, https://doi.org/10.1021/nl1023854.
[44] F. Paleari, *First-principles approaches to the description of indirect absorption and luminescence spectroscopy: exciton-phonon coupling in hexagonal boron nitride*, Ph.D. thesis, University of Luxembourg (2019).
[45] F. Guinea and N. R. Walet, Physical Review B **99**, 205134 (2019), arXiv:1903.00364.
[46] N. R. Walet and F. Guinea, Physical Review B **103**, 125427 (2021), arXiv:2011.14237.
[47] K. Yao, N. R. Finney, J. Zhang, S. L. Moore, L. Xian, N. Tancogne-Dejean, F. Liu, J. Ardelean, X. Xu, D. Halbertal, K. Watanabe, T. Taniguchi, H. Ochoa, A. Asenjo-Garcia, X. Zhu, D. N. Basov, A. Rubio, C. R. Dean, J. Hone, and P. J. Schuck, Science Advances **7**, eabe8691 (2021).
[48] L. Wirtz and A. Rubio, "Optical and vibrational properties of boron nitride nanotubes," in *B-C-N Nanotubes and Related Nanostructures* (Springer New York, New York, NY, 2009) pp. 105–148.
[49] R. M. Ribeiro and N. M. R. Peres, Phys. Rev. B **83**, 235312 (2011).
[50] N. Berseneva, A. Gulans, A. V. Krasheninnikov, and R. M. Nieminen, Phys. Rev. B **87**, 035404 (2013).
[51] F. Hüser, T. Olsen, and K. S. Thygesen, Phys. Rev. B **87**, 235132 (2013).
[52] F. Hüser, T. Olsen, and K. S. Thygesen, Phys. Rev. B **87**, 235132 (2013).